

# Precise structure and polarization determination of $\text{Hf}_{0.5}\text{Zr}_{0.5}\text{O}_2$ with electron ptychography

Received: 13 November 2025

Accepted: 2 February 2026

Published online: 14 February 2026

 Check for updatesXiaoyue Gao<sup>1,2,8</sup>, Zhuohui Liu<sup>3,8</sup>, Bo Han<sup>1,2</sup>, Xiaowen Zhang<sup>1,2</sup>, Ruilin Mao<sup>1,2</sup>, Ruochen Shi<sup>1,2</sup>, Ruixue Zhu<sup>1,2</sup>, Jiangbo Lu<sup>4</sup>, Tao Wang<sup>2</sup>, Kuijuan Jin<sup>3</sup>, Jiade Li<sup>1,2</sup>✉, Chen Ge<sup>3</sup>✉ & Peng Gao<sup>1,2,5,6,7</sup>✉

$\text{Hf}_{0.5}\text{Zr}_{0.5}\text{O}_2$  emerges as a promising candidate for next-generation ferroelectric memories and transistors. However, the intrinsic nature of its ferroelectricity remains a subject of debate, primarily stemming from challenges in the precise characterization of nanoscale polycrystallinity and multiphase coexistence. Here, we investigate substrate-free  $\text{Hf}_{0.5}\text{Zr}_{0.5}\text{O}_2$  films using multislice electron ptychography, achieving a resolution of 25 picometers with capabilities for oxygen imaging, depth resolution, and vacancy quantification. Precise measurements reveal that the polarization displacement in ferroelectric phase is  $\sim 56 \pm 6$  picometers (corresponding to a polarization  $\sim 34 \pm 4 \mu\text{C}/\text{cm}^2$ ). We further identify significant polarization suppression near grain boundaries, while there is negligible change in the  $180^\circ$  neutral domain walls. Furthermore, we demonstrate the existence of the  $180^\circ$  head-to-head charged domain wall in  $\text{Hf}_{0.5}\text{Zr}_{0.5}\text{O}_2$ , which is confined within a single unit cell layer. At such a charged domain wall, the atomic displacement is reduced to  $\sim 4$  picometers, with oxygen vacancies accumulating up to 20%. Notably, the polar layers neighboring the  $180^\circ$  head-to-head charged domain wall remain unchanged. The precise determination of these structural features with ultrahigh spatial resolution offers critical information for optimizing and designing new hafnium-based ferroelectric devices.

$\text{Hf}_{0.5}\text{Zr}_{0.5}\text{O}_2$  (HZO) has gained widespread attention due to its robust ferroelectricity at room temperature and excellent compatibility with complementary metal-oxide-semiconductor (CMOS) technology<sup>1–3</sup>. As a continuous solid solution of  $\text{HfO}_2$  and  $\text{ZrO}_2$ , HZO benefits from Zr-induced stabilization of the ferroelectricity and exhibits the highest remanent polarization in the  $\text{Hf}_{1-x}\text{Zr}_x\text{O}_2$  series<sup>4–8</sup>. This material is also regarded as a promising candidate for the next generation of

ferroelectric random-access memories (FeRAMs) and ferroelectric field-effect transistors (FeFETs)<sup>7,9,10</sup>. For example, its switchable ferroelectricity in 1 nm-thick films (surpassing traditional perovskites) for high-density FeRAMs and negative capacitance for low-power FeFETs have been demonstrated<sup>1,5,7,11</sup>. To further optimize core applications like FeRAMs (enhancing storage density and switching speed) and FeFETs (improving power efficiency and operation stability), it is

<sup>1</sup>International Center for Quantum Materials, School of Physics, Peking University, Beijing, China. <sup>2</sup>Electron Microscopy Laboratory, School of Physics, Peking University, Beijing, China. <sup>3</sup>Beijing National Laboratory for Condensed Matter Physics, Institute of Physics, Chinese Academy of Sciences, Beijing, China.

<sup>4</sup>School of Physics and Information Technology, Shaanxi Normal University, Xi'an, China. <sup>5</sup>Tsientang Institute for Advanced Study, Zhejiang, China. <sup>6</sup>Interdisciplinary Institute of Light-Element Quantum Materials and Research Center for Light-Element Advanced Materials, Peking University, Beijing, China.

<sup>7</sup>Collaborative Innovation Center of Quantum Matter, Beijing, China. <sup>8</sup>These authors contributed equally: Xiaoyue Gao, Zhuohui Liu.

✉ e-mail: [jqli@pku.edu.cn](mailto:jqli@pku.edu.cn); [gechen@iphy.ac.cn](mailto:gechen@iphy.ac.cn); [pgao@pku.edu.cn](mailto:pgao@pku.edu.cn)

essential to seek and investigate novel polarization structures at the nanoscale in HZO, such as  $180^\circ$  charged domain walls (CDWs)<sup>12–14</sup>. These  $180^\circ$  CDWs enable the opposite polarization (head-to-head or tail-to-tail) at the unit cell scale, where charge accumulation at the walls stabilizes sharp domain boundaries<sup>14,15</sup>. Such charge-mediated stabilization significantly lowers the switching barrier, thereby offering a solid physical basis for realizing high-density and low-power ferroelectric devices<sup>14–17</sup>. However, although theoretical predictions suggest that these  $180^\circ$  CDWs can exist in hafnium-based oxide, experimental observations are still lacking<sup>14,16,17</sup>.

Besides, the origin of HZO's ferroelectricity itself remains a topic of ongoing discussion<sup>18–22</sup>. The mainstream view is that the ferroelectricity in hafnium oxide films arises from the ferroelectric orthorhombic phase (O111 phase, space group  $Pca2_1$ ) supported by experimental evidence<sup>3,21,23–25</sup>, but other mechanisms (e.g., polar rhombohedral phase) are also proposed<sup>2,22,26–29</sup>. Therefore, accurately analyzing the intrinsic atomic structures of HZO, e.g., oxygen configurations and domain walls (DWs), is crucial for understanding the nature of ferroelectricity. However, such analysis is typically challenging due to its substrate effects and polycrystalline nature<sup>16,30–32</sup>. On the one hand, the substrate effects can lead to lattice clamping<sup>29,33</sup> and interfacial charge screening<sup>2,34</sup> in the hafnium-based oxide films, which hinder the detection of intrinsic ferroelectric nature. They can also introduce structural artifacts affecting the accurate atomic-scale structural analysis. Recent advances in freestanding membranes can mitigate these issues and enable precise atomic characterization in HZO<sup>13,21,30</sup>. On the other hand, the polycrystalline nature leads to different atomic-scale features present even within a single grain at the nanoscale, including surfaces, grain boundaries (GBs) and DWs, necessitating high spatial resolution characterization. Conventional high-angle annular dark field scanning transmission electron microscopy (HAADF-STEM, with typical resolution  $\sim 60$  pm) fails to detect low atomic number oxygen, whereas oxygen sensitive transmission electron microscopy (TEM) techniques are highly sensitive to imaging conditions (e.g., specimen mistilt, thickness variation and residual aberrations), which can easily lead to artifacts<sup>35–38</sup>. Furthermore, traditional diffraction-based techniques like position-averaged convergent beam electron diffraction (PACBED) and 4D-STEM methods have been widely used for polarization analysis in ferroelectrics<sup>23,39–42</sup>. However, these methods are limited by finite spatial resolution, challenges in polarization quantification, and lack of depth information. Fortunately, state-of-the-art multislice electron ptychography (MEP) offers superior resolution ( $\sim 20$  pm) and uniquely enables simultaneous imaging of cation and oxygen positions, depth information retrieval and specimen mistilt correction, which is ideal for atomic structure quantification<sup>43–52</sup>.

Herein, we used MEP to achieve ultra-high-resolution imaging ( $\sim 25$  pm) of polycrystalline HZO freestanding films. We determined the atomic structures of multiple phases and measured the intrinsic polarization displacement of HZO to be  $-56 \pm 6$  pm, corresponding to a polarization of  $-34 \pm 4$   $\mu\text{C}/\text{cm}^2$ . At GBs, significant polarization suppression up to the fourth polar layer was observed. Moreover, we observed a  $180^\circ$  head-to-head (H-H) CDW in HZO. Such a CDW is a one-dimensional line, i.e., its width is only about one unit cell, and confined within a single polar layer. The atomic polar displacement at the CDW is reduced to  $\sim 4$  pm, accompanied with  $\sim 20\%$  oxygen vacancies ( $V_{\text{O}}$ ) based on the depth-resolved reconstruction. In contrast, no detectable polarization changes are observed in the neighboring polar layers of the  $180^\circ$  H-H CDW. These findings provided basic insights into the HZO ferroelectricity and related applications.

## Results

### Various phases in HZO

The 5-nm-thick HZO freestanding film shown in Fig. 1a was studied to eliminate the influence of phenomena such as interface effects, grain overlap, and sample preparation damage<sup>33,34</sup>, thereby ensuring precise

structural analysis. The morphology distribution of grains shown in Fig. 1b, with an average size of  $\sim 10$  nm, is consistent with previous studies<sup>30</sup>. The P-E hysteresis measurement (Fig. 1c) shows that polarization of the film is  $\sim 16$   $\mu\text{C}/\text{cm}^2$ . Experimental setup for MEP technique is schematically shown in Fig. 1d. The sample was scanned with an overfocused probe and collected diffraction patterns (Figure. S1) via a pixelated detector, and the datasets were then reconstructed using the MEP algorithm with post-alignment method correcting slight mistilt (Figure. S1) to resolve the 5 nm HZO film in three-dimensions (Fig. S2)<sup>44–46,53</sup>. The reconstructed real-space resolution is  $\sim 25$  pm (Fig. 1e), which is much better than that of HAADF image [ $\sim 61$  pm, Fig. S3 in Supplementary Material (SM)]. The reconstructed probe structures (Figure. S4 in SM) are robust and consistent with those reported in previous studies<sup>48,54–56</sup>. Projected MEP images in Fig. 1f show multiple phases of HZO including the ferroelectric (FE) phase, the antiferroelectric (AFE) phase, the monoclinic-like (M') phase and the cubic (C) or tetragonal (T) phase, in excellent agreement with the simulated reconstructions and atomic model in Fig. S5. These abundant results as well as the monoclinic (M) phase (Figs. S6 and S7 in SM) unveiled several key discoveries. 1) By combining MEP images with corresponding simulations, we confirmed that the intrinsic FE phase in HZO adopts O phase with space group  $Pca2_1$ . 2) We identified the AFE nature of the M phase along the [100] direction (Figure. S7 in SM), with notable variations in displacements between neighboring layers. 3) We also captured a novel {010}-Hf/Zr antiphase boundary (APB) defect in the M phase, which has not been previously reported. The crystal structure demonstrate its significant influence on the nearby polarization (see Figure. S7 in SM for details).

Based on the reconstructed atomic images shown in Figs. S8 and S9 of the SM, the lattice structures of various phases were analyzed in detail (Fig. 1f). The FE phase features centrosymmetric non-polar oxygen atoms (O1) and non-centrosymmetric polar oxygen atoms (O2) with measured interatomic distances of  $41 \pm 2$  pm and  $60 \pm 5$  pm, respectively. The corresponding O1 and O2 distances for the AFE and M' phases are summarized in Fig. 1f representing the statistical distributions obtained from our measurements. The extracted O phase lattice parameters fall within the range reported in previous experimental and computational studies of ferroelectric HZO (Table S1 in SM)<sup>57–61</sup>. It should be mentioned that the MEP images cannot differentiate whether the metallic sites are occupied by Zr or Hf due to the limitation of depth resolution. In addition, the angle of adjacent metallic atoms is  $\sim 75^\circ$  in M' phase and  $70^\circ$  in M phase, providing more details of the coexistence of M' and M phases including strain effects and atomic relaxations (discussed in Fig. S6 of the SM). For the C/T phase, the structural parameters (indistinguishable from  $c$ -axis) are consistent with previous studies<sup>62</sup>. Analysis of nine MEP images totaling  $70 \times 70$  nm<sup>2</sup> (Figure. S9 in SM) revealed that the FE-O phase ( $\sim 50\%$ ) dominates over the AFE-O ( $\sim 21\%$ ) and M ( $\sim 23\%$ ) phases. Minor phases M' and T/C are rarely observed, typically appearing as single atomic layers within O phase grains.

### Polarization in bulk and grain boundaries

In Fig. 2a, we show a FE grain image along the [010] axis and mapped the distribution of displacements between cation and oxygen. Statistical analysis of O phase grains (Fig. 2b) suggests that the polarization displacement is  $-56 \pm 6$  pm with corresponding spontaneous polarization ( $P_s$ ) of  $34 \pm 4$   $\mu\text{C}/\text{cm}^2$ , consistent with the reported theoretical values<sup>19,20</sup>. The distribution near the zero point in the histogram originates from the non-polarized layers, and in-plane displacement ( $0.8 \pm 3$  pm, see Fig. S10 in SM) along the  $a$ -axis indicates that the polarization direction is along the  $c$ -axis. Our extensive measurements show that even in the pristine films, grains with uniform polarization direction (Fig. 2a) are very rare. Most O phase grains exhibit a mixture of FE and AFE phases, as shown in Fig. 2c. This is reasonable due to the similar energies of the FE and AFE phases, along with the

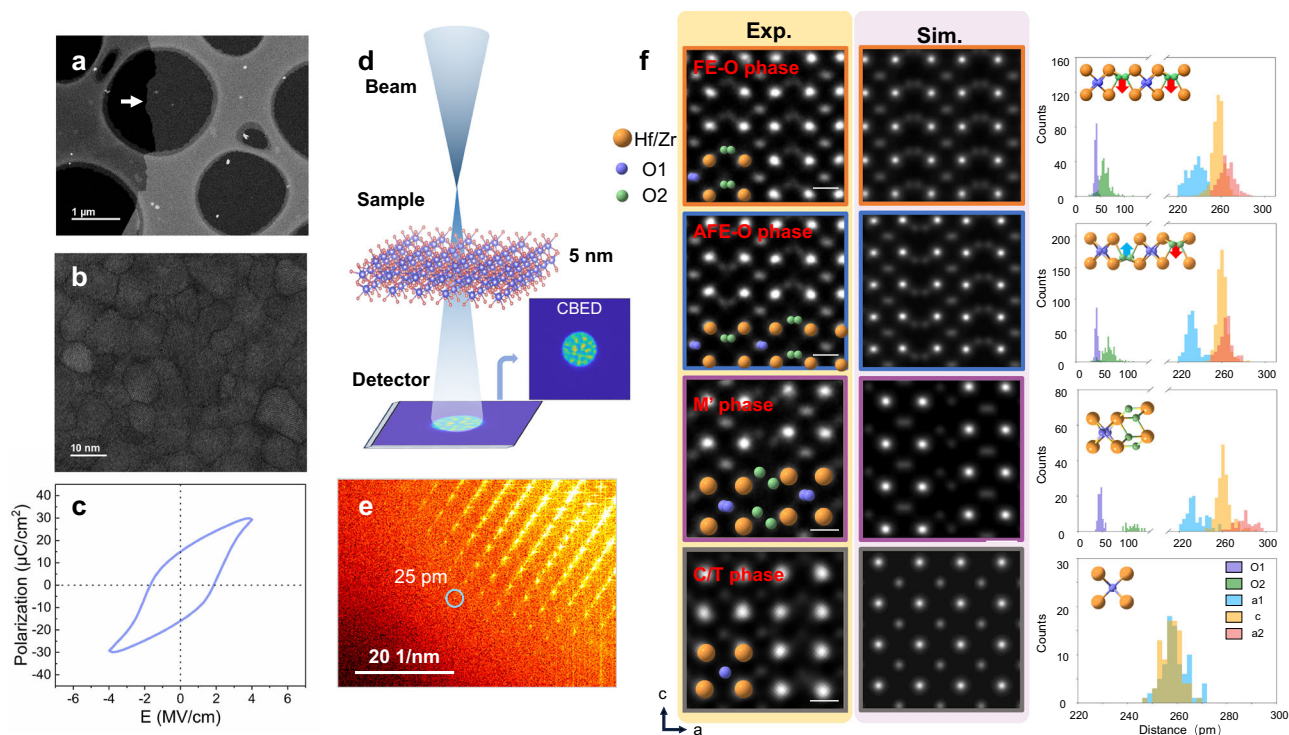


**Fig. 1 | Imaging atomic structures of HZO freestanding thin film.** **a** Low-magnification plan-view HAADF-STEM of HZO freestanding film. White arrow indicates sample's edge. **b** HAADF-STEM image shows the grain distribution of film. **c** Polarization-electric field (**P-E**) hysteresis loops at 10 kHz. **d** Experimental setup of MEP. The inset is a convergent beam electron diffraction (CBED) image from dataset. The crystal figure is generated using VESTA<sup>87</sup>. **e** Fourier transform of the phase image in Fig. S3 of the SM, as dashed circle denotes real space resolution of 25 pm. **f** Projected phase images from multislice electron ptychographic reconstructions of experiments (left side) overlapped with atomistic structure models, the corresponding simulated reconstructions (middle side), and the

experimental histograms of lattice parameters for each phase (right side). From top to bottom are FE phase, AFE phase, M' phase and C/T phases. Scale bar, 0.2 nm. FE phase (O1 is  $41 \pm 2$  pm, O2 is  $60 \pm 5$  pm, a1 is  $235 \pm 6$  pm, c is  $257 \pm 3$  pm and a2 is  $265 \pm 6$  pm, polarization is  $56 \pm 6$  pm), AFE phase (O1 is  $44 \pm 3$  pm, O2 is  $68 \pm 6$  pm, a1 is  $233 \pm 5$  pm, c is  $261 \pm 4$  pm and a2 is  $264 \pm 5$  pm, polarization is  $56 \pm 6$  pm), M' phase (O1 is  $46 \pm 4$  pm, O2 is  $113 \pm 6$  pm, a1 is  $235 \pm 6$  pm, c is  $261 \pm 5$  pm and a2 is  $282 \pm 5$  pm), and C/T phase (a1 is  $259 \pm 5$  pm and c is  $258 \pm 3$  pm). O1 is the distance of O1 atom pairs and O2 is the distance of O2 pairs; a1 and a2 are the half-lattice constants of *a*-axis in the sublattice of O1 and O2, respectively; c is half-lattice constant of *c*-axis.

independently switchable characteristics of polar layers<sup>20</sup>. The polarization magnitude mapping in Fig. 2d shows no detectable polarization variation across the opposite polarization directions (Fig. 2e), i.e., 180° DWs. But there is significant polarization suppression near GBs as shown in Fig. 2f. Partial oxygen ions in polarized layers near the GBs are relaxed towards the center position but still non-overlapping to each other, whereas the lattice along the *c*-axis with no obvious decrease (Fig. S10 in SM), resulting in polarization suppression throughout the entire relaxed polar layer. This typical polarization suppression extended beyond the outermost three polar layers (Fig. 2f), the underlying mechanism of suppression is usually very complicated at GBs, but our observation provides critical clues that reconstructed region near GBs clearly reveals the presence of  $V_O$ . Electron energy loss spectroscopy (EELS) measurements (Fig. S11 in SM) further confirm significant and widespread  $V_O$  accumulation at these boundaries. Specifically, the blurring of O-K edge doublets in EELS spectra indicates a higher concentration of  $V_O$  at GBs<sup>63–65</sup>, suggesting their potential role in modulating local polarization behavior.

### 180° head-to-head charged domain wall

As common intrinsic defects in FE materials,  $V_O$  play a crucial role in influencing the FE properties of materials and device performance<sup>66–68</sup>. Notably, computational studies have investigated the formation and structures of the 180° CDW in hafnium-based oxides and proposed the  $V_O$  as a key contributing factor<sup>14,16,17</sup>, but experimental evidence has remained lacking until now. Inspired by the above observations, we further report an experimental observation of a localized 180° H-H CDW near the GBs in HZO (Fig. 3a). The corresponding HAADF image

(Figure. S12 in SM) with a larger field of view confirms that the CDW exists near the GB. The atomic structure of the 180° H-H CDW indicated that there are two oxygen columns (i.e., col. 5 and 5') within the CDW's unit cell. The depth profile of these oxygen columns (Fig. 3b) revealed the presence of  $V_O$  and the distortion of the columns, especially for the columns 5 and 5'. We further analyzed the polarization,  $V_O$ , and the lattice constants of the 180° H-H CDW structure based on the MEP result. Specifically, we observed single-unit-cell layers with head-to-head polarization (highlighted by the red box in Fig. 3a). As shown in Figs. 3c and S13 in SM, there are a non-polar unit cell at the center of the CDW with almost equal but opposite polarization on either side (Layer\_2) along depth. The polarization suppression observed in the right-hand region primarily arises from the proximity to GBs, as discussed above. The polar layers (i.e., Layer\_1 and Layer\_3, black and yellow boxes in Fig. 3a) adjacent to the 180° H-H CDW retain bulk-like polarization. They are not affected by the CDW itself. The coexistence of FE and AFE phases within a single grain further supports the scale-free ferroelectric nature of hafnium oxide<sup>20</sup>. The phase intensity of the O columns in Fig. 3d clearly reveals pronounced reduction at both the 180° H-H CDW and GBs. Quantitative analysis (Fig. 3d) shows that the concentration of  $V_O$  within the cell at the CDW reaches up to 20%, whereas the concentration near the GBs is approximately 7–12%. Notably, we found that  $V_O$  are not only confined to the DW (the non-polar unit cell) but also exist in at least one polar unit cell on both sides of the CDW. Furthermore, the extracted lattice constants around the CDW with no significant changes (Figs. 3e and S12 in SM) indicate no notable structural alterations. These experimental results reveal a clear spatial correlation between oxygen vacancy accumulation and local

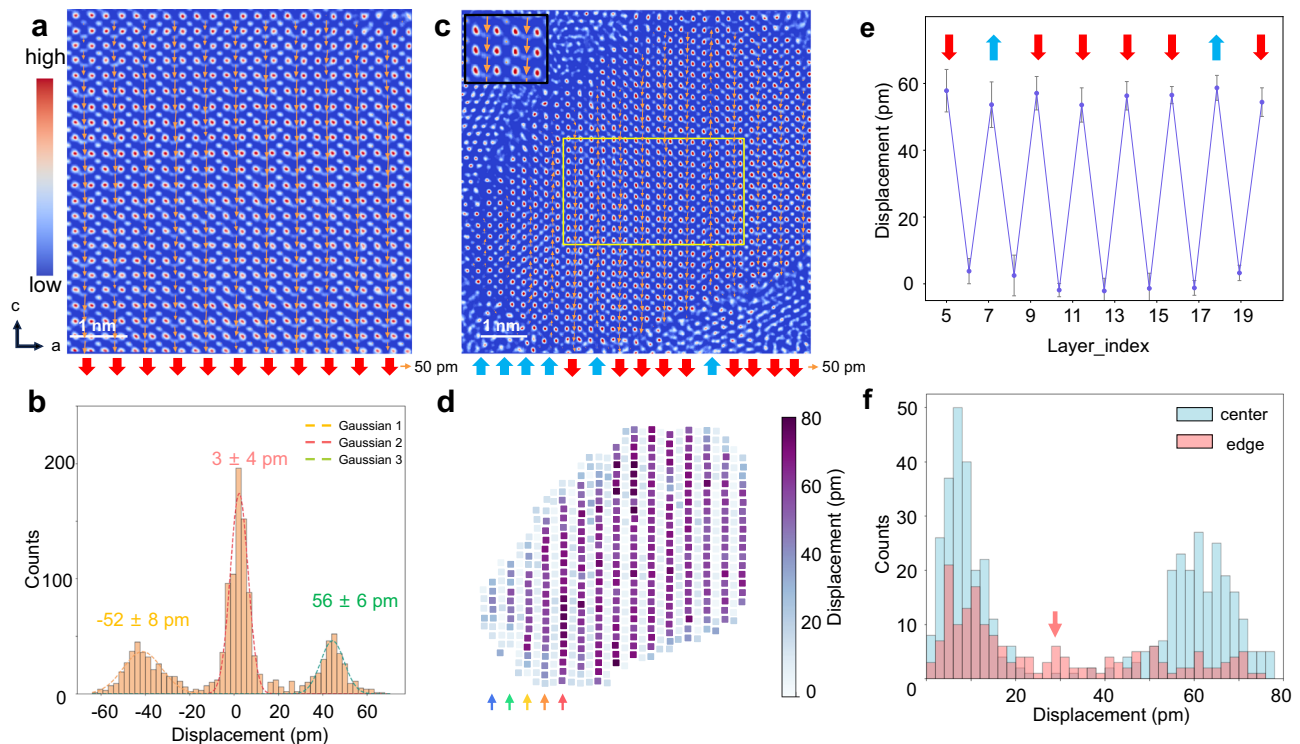


**Fig. 2 | Ferroelectric polarization mapping.** **a** Projected MEP phase image of a FE grain along [010] direction with displacement arrows overlapped. **b** Statistical histogram of polarization displacements in O phase HZO grains. The fit curves represent Gaussian fitting. **c** Projected MEP phase image from a FE-AFE mixed grain with displacement arrows overlapped. Inset represents enlarged region of polarization mapping. The blue and red arrows in (a) and (c) indicate the direction of

polarization in each polar layer. **d** The displacement magnitude map corresponding to (c). **e** The mean polarization of every polar layer extracted from yellow dashed-line region in (c). **f** Displacement distributions from the edge (red, three outermost layers of the grain) and interior (blue, the rest center part of the grain excluding the edge) of grain shown in (c). The red arrow indicates the polarization suppression near the grain boundaries.

ferroelectric polarization behavior in HZO, particularly at grain boundaries and the 180° H-H CDW, directly demonstrating their coexistence at the atomic scale. Detailed understanding of how the vacancies exactly influence polarization stabilization and domain-wall formation requires further in-depth investigation.

## Discussion

Precise atomic structure measurements of the freestanding HZO films revealed the FE phase, DWs, and polarization suppression at GBs, which significantly enhances our understanding on the FE properties of HZO. By accurately fitting the atomic position with custom-trained models (Fig. S14) and measuring the polarizations, we confirmed that the intrinsic FE phase of HZO originates from the orthorhombic structure (space group  $Pca2_1$ ), characterized by alternating polar and non-polar layers, which is in contrast with the traditional perovskite-type ferroelectrics. The polarization of the FE phase, obtained from polarization displacement measurement ( $56 \pm 6$  pm), is  $-34 \pm 4 \mu\text{C}/\text{cm}^2$ , which aligns well with previous theoretical values<sup>19,20</sup>. However, most reported experimental values are below  $30 \mu\text{C}/\text{cm}^2$ <sup>225,69</sup>, and our P-E hysteresis measurement also reflects this trend ( $16 \mu\text{C}/\text{cm}^2$ ), which could be attributed to the coexistence of non-polar and anti-polar structures in the films. Due to the negligible energy difference between the FE-O and AFE-O phases<sup>20</sup>, they always coexist within a single grain, but a higher presence of the FE-O phase in the pristine film is reasonable, as the phase distribution is strongly influenced by factors, like dopants, strain, and defect chemistry, preferentially stabilize the FE-O phase in HZO thin films<sup>5,6,8</sup>. In contrast with perovskite ferroelectrics, no significant changes in lattice constant or polarization were observed between the two phases. Our precise measurements show that the polarization suppression, commonly observed at GBs (with displacements reduced up to 13 pm, -77%), extends across

multiple polar layers (Fig. S10 in SM), with both the magnitude and range exceeding those reported previously<sup>21</sup>. Our EELS and imaging results suggest this is directly attributed to the widespread  $V_o$  at GBs, which play a potential role in modulating local polarization behavior by disrupting the local electrostatic environment and bonding states. Although the [111] direction is one of the most commonly dominant orientation in films, direct imaging of oxygen atoms from this direction is challenging due to the closest projected distance between oxygen and cation is less than  $75 \text{ pm}$ <sup>30,70</sup>. Benefiting from the ultra-resolution of MEP, we also successfully image the oxygen atoms (Figs. S15 and S16 in SM) from the O-[111] orientation. Due to the continuous solid-solution nature<sup>5</sup> of  $\text{Hf}_{0.5}\text{Zr}_{0.5}\text{O}_2$ , the contrast of metallic sites in MEP images does not allow direct discrimination between Hf and Zr atoms. Atomic-resolution EDS mapping (Fig. S17) confirms a uniform Hf/Zr distribution with an approximately 1:1 ratio across the film, consistent with random cation occupancy feature.

More importantly, we directly observed the 180° H-H CDW, which was extensively investigated in theoretical studies<sup>14,16,17</sup>. Our comprehensive and precise measurements, especially the capability of quantifying  $V_o$  with three dimensions, highlight a defect-driven mechanism distinct from traditional ferroelectrics<sup>68</sup>. In traditional systems (e.g.,  $\text{PbTiO}_3$ ), DWs are typically stabilized by long-range lattice strain or dipolar interactions that differs from that of the CDW in the HZO system<sup>71,72</sup>. However, in our multislice experiments in HZO, firstly, we reveal that there are localized  $V_o$  (~20%) near the 180° H-H CDW. This observation is consistent with previous theoretical predictions, which suggests that the presence of  $V_o$  alters the conduction band structure, thereby enhancing the stability of H-H CDW configuration<sup>16,17</sup>. The  $V_o$  act as active structural mediators by suppressing polarization near GBs (Figs. 2c and S11 in SM) and modifying the polarization configuration (e.g., the 180° H-H CDW), rather than passive pinning centers.

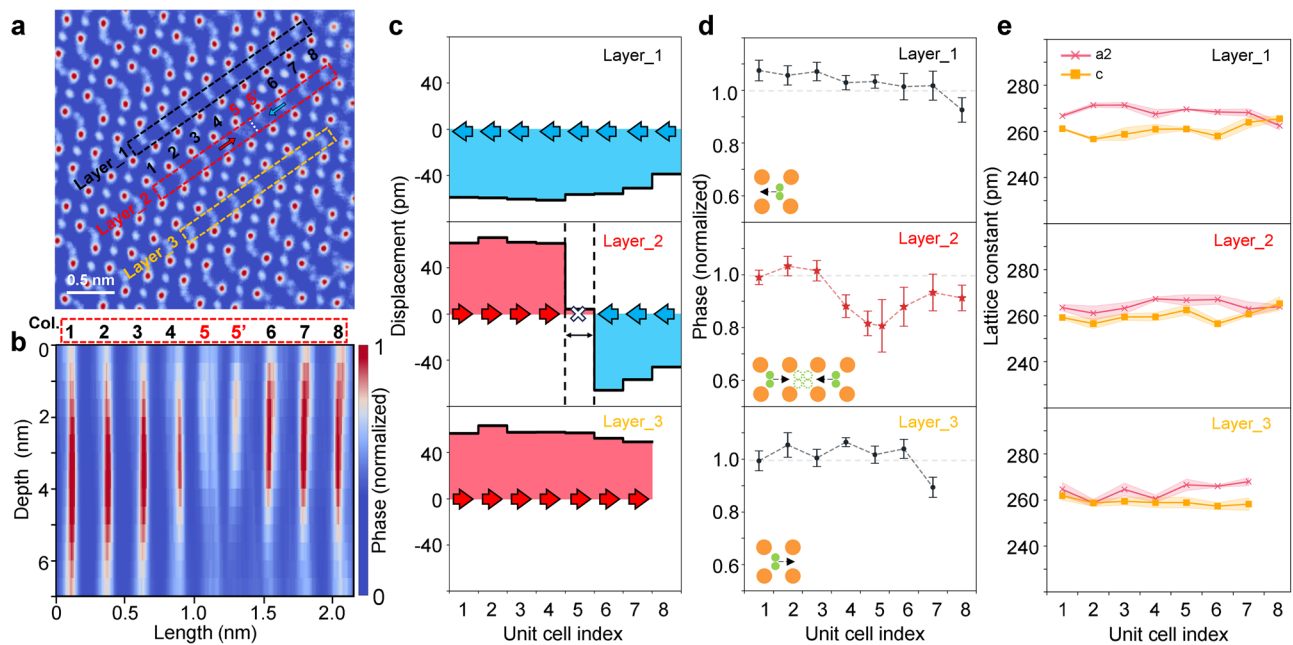


**Fig. 3 | 180° head-to-head charged domain wall with oxygen vacancies.** **a** Experimental projected MEP phase image of the 180° H-H CDW (as noted by red box region). The colored arrows indicate the polarization directions across the CDW. **b**, Depth profile of the oxygen columns marked in (a). **c** Polarization of the layers that marked with the corresponding colored dashed-boxes in (a) (see Methods). The blue and red arrows indicate the polarization directions of (a). **d** The

depth-averaged phases of the O columns in the three layers. The error bars present the standard deviations along the depth. **e** The corresponding half-lattice constants of the three layers. The shadow regions present the standard deviations along the depth. The unit cell indexes represent the direction of unit cells in (a) plotted from left bottom to right up.

Secondly, the unaltered lattice constants around the CDW (Figs. 3e and S12 in SM) indicate the decoupling of CDW stability from long-range lattice distortion, reinforcing that sub-unit cell scale dipoles are individually switchable in hafnium oxides<sup>20</sup>. Lastly, the width of the H-H CDW is merely one unit-cell, whereas the CDWs in conventional perovskite oxides are typically much wider (spanning several unit cells or nanometers)<sup>72,73</sup>. Polar layers flanking the CDW retain bulk-like polarization, demonstrating that HZO sustains ferroelectricity at sub-nanoscale where traditional ferroelectrics fail<sup>74,75</sup>. In essence, the experimental observation of 180° H-H CDW in HZO identifies a defect-mediated stabilization pathway that diverges from traditional ferroelectric paradigms<sup>68</sup>, offering both mechanistic insights and a roadmap for device design. Furthermore, MEP enables us to successfully identify the 180° H-H CDW in HZO freestanding films and provides a solid basis for further domain-wall studies. Future work could focus on other domain structures, specifically 90° DWs that have been previously observed in TiN/HZO/TiN capacitors<sup>76,77</sup>, to advance HZO domain engineering.

In summary, we investigate the intrinsic atomic structures and defects in HZO freestanding films with MEP, determining that the intrinsic polarization magnitude of HZO is  $-56 \pm 6$  pm. We find substantial polarization suppression occurring around GBs and extending across multiple polar layers. Furthermore, we report the experimental observation of the 180° H-H CDW with a one-dimensional configuration, i.e., one unit cell in width, and is confined within a single polar layer. Depth-resolved reconstruction further demonstrates that such a H-H CDW is associated with a considerable amount of  $V_O$  (~20%) accumulating at the DW. These results highlight the structural complexity of HZO and provide valuable insights into optimizing hafnium-based materials.

## Methods

### Sample preparation

The HZO films with 5 nm thickness were synthesized as HZO/La<sub>0.8</sub>Sr<sub>0.2</sub>MnO<sub>3</sub> (LSMO) heterostructures on single crystal SrTiO<sub>3</sub> (STO)

through pulsed laser deposition (PLD) method using a XeCl laser ( $\lambda = 308$  nm) and the deposition temperatures was 780 °C. The laser energy fluence was 1.75 J/cm<sup>2</sup>, and the repetition rates used for both films were the same (2 Hz). The deposition rate of films was calibrated by X-ray Reflection. After growth, the HZO films were released from the STO substrate by selective etching of the sacrificial LSMO layer. The unclamped thin films were removed from the substrate by slowly dipping it into deionized water. A homemade copper wire loop was used to catch the freestanding HZO membranes from the water surface, held in place by a thin water layer inside the loop. The films were then transferred to target substrates on a 95 °C hot plate. The freestanding HZO films remained on the copper TEM grids (with holey carbon supporting layer) after water evaporated.

### Experimental 4D-STEM datasets acquisition

The 4D-STEM experiments and HAADF imaging were operated at 300 kV on a double-aberration-corrected JEOL JEM-ARM300F2 microscope. Considering the thickness of film, convergence semi-angle ( $\alpha$ ) of 32.8 mrad was selected for all datasets<sup>78</sup>. We adopted an overfocus probe -10 nm above the sample surface to collect the datasets. The electron probe current used was approximately 20 pA. The 4D-STEM datasets were recorded with 0.819 mrad/pixel by using a Medipix3 MerlinIR direct electron pixelated detector with 256×256 pixels. The datasets were acquired using a dynamic range of 12-bit in electron-counting mode with 0.617 ms dwell time per diffraction pattern with scan step size about 0.304 Å. The first two rows of raw datasets were deleted to avoid scan noise.

### Ptychographic reconstructions and data analysis

Ptychographic reconstructions were performed based on the mixed-state multislice algorithm available in the fold-slice package<sup>44,45,79</sup>, using 5 slices with slice thickness of 1 nm. For the reconstruction in Fig. 3, we used 0.5 nm/slice for depth analysis. For each dataset, multiple reconstructions were iterated to improve the resolution with each undergoing more than 600 iterations. We corrected the mistilt in

experiment by performing post-alignment of all slices<sup>46</sup>. As illustrated in Supplementary Fig. 13, based on the position averaged convergent beam electron diffraction (PACBED), we chose grains with tiny mistilt for further reconstruction. For our ultrathin samples, Kikuchi patterns were difficult to distinguish, where mistilt was quantified via analysis of center shift between the zero-order Laue zone (ZOLZ) and the first-order Laue zone (FOLZ)<sup>39,80</sup>. The mistilt of FOLZ is estimated ~ 6 mrad (Fig. S1 in SM) and corresponding offset for sample ~ 6 pm/nm. The corrected shift (Fig. S1 in SM) proves that the mistilt was considered and corrected effectively. The probe positions were updated with relaxed constraint applied about every 50 iterations<sup>79</sup>. The moderate regularization parameters ranging from 1 to 0.5 were applied for high-quality reconstructions<sup>44,46</sup>. The step of least square in least square maximum likelihood (LSQ-ML) algorithm was set 0.1 for initial convergence and decrease to 0.05 for final refine<sup>44</sup>. We considered the point spread function (PSF) effects of the detector we used.

Based on the complex structures of HZO, AtomAI<sup>81</sup> and Atomap<sup>82</sup> were used to fit and analyze the atomic positions, intensities and structures. The atomic positions were predicted using the custom-trained model in AtomAI and then Atomap was used for 2D-Gaussian fitting to refine the positions ensuring precision. First, we trained custom models with a ResHedNet-like network for semantic segmentation of atomic images in AtomAI with simulated and experimental HZO images. To enhance the robustness especially for blurred atoms, we applied various image “distortions” (e.g., noise, blurring, and zoom) to the cropped images, as illustrated in Fig. S16. The network was trained to process these input images and produce outputs of clean, circular-shaped “blobs” on a uniform background, from which the  $(x, y)$  centers of atoms could be identified. The training process involved 1000 epochs to achieve convergence, as shown in Fig. S14. We further refined the cation atomic positions using Atomap in two steps: 1. Center of Mass Calculation: Preliminary refinement of atom positions; 2. 2D-Gaussian Fitting: Every atomic column was further refined with an elliptical 2D-Gaussian function:

$$f(x, y) = \frac{A}{2\pi\sigma_x\sigma_y} \exp\left(-\frac{(x-\mu_x)^2}{2\sigma_x^2} - \frac{(y-\mu_y)^2}{2\sigma_y^2}\right)$$

where the  $A$  is the magnitude,  $(\mu_x, \mu_y)$  is the position,  $\sigma_x$  and  $\sigma_y$  are the standard deviation in  $x$  and  $y$  direction respectively. For light elements, we accounted for the lower intensity by subtracting the Gaussian of cations from the images. The positions of light elements were then refined in same way as the cation positions. All functions used for refinement are built-in features of Atomap with additional details available in reference<sup>82</sup>. The O1 distances were accurately determined by fitting columns with Gaussian functions. For polarization analysis, the obtained relative displacement  $\delta$  of cations and anions was used to calculate polarization by  $P_s = \frac{e}{V} \sum \delta_i Z_i$ , where  $e$  is the electronic charge,  $V$  is the volume of unit cell and  $Z_i$  is Born charge values,  $\delta$  is displacement/shift of atom ( $i$ ) from their centrosymmetric position<sup>83</sup>. The Born charge value for the A site is 5.15, which is derived as the mean value of 5.0 for Hf and 5.3 for Zr<sup>84,85</sup>. The polarization of the CDW was determined by calculating the center position of the two pairs of O columns as the mean anion position in the cell of the CDW. We choose the smallest polarization in the outermost polar layer to obtain the suppression maximum of 13 pm indicated by blue arrow in Fig. 2d. The normalization in the study is normalized based on the corresponding mean value.

### Simulation of 4D-STEM datasets

All simulated 4D-STEM datasets were implemented with abTEM<sup>86</sup> using Kirkland’s parametrization of atomic potentials. Thirty frozen phonon configurations were averaged to account for the thermal diffuse scattering. Parameters such as beam energy, sample thickness, scan step, defocus and convergence semi-angle from the experiments were used in the simulations. The aberrations were set to zero for simplicity.

All simulated datasets were generated under the assumption of an infinite electron dose, meaning that Poisson noise was not introduced, aiming to preserve clear structural details in the ptychographic reconstructions. Additionally, the datasets (i.e., the collected diffraction patterns) were Gaussian-blurred to account for source size.

### STEM-EELS

The energy loss spectra were acquired at a Nion U-HERMES200 electron microscope equipped with both the monochromator and the aberration corrector operated at 60 kV. The probe convergence semi-angle was 35 mrad, while the collection semi-angle was 25 mrad. The core-level EEL spectrum was recorded as spectrum image with 1.6 nm × 8 nm and 0.08 nm per pixel. EEL spectra were processed using the Gatan Microscopy Suite and custom-written MATLAB code. The spectra were summed along the direction parallel to the interface to obtain the line-scan data with a good signal-to-noise ratio.

### P-E hysteresis measurement

The ferroelectric P-E hysteresis loops were measured using a capacitor-like structure comprising a Pt/HZO/LSMO heterostructure. A precision multiferroic analyzer (RADIANT Tec. Inc.) was employed to measure the polarization intensity of the HZO films on a macroscopic scale. A tungsten probe was used for P-E measurements, with a frequency of 10 kHz for the triangular pulses applied to switch the polarization of the ferroelectric layer. The analyzer applied a periodic electric field sweep while measuring the current/charge response, integrating the displacement current to calculate the polarization ( $\mathbf{P}$ ), which was related to the applied electric field ( $\mathbf{E} = V/t$ ), where  $t$  is the thickness of the ferroelectric layer. Consequently, the P-E loop was generated, elucidating the ferroelectric properties of the HZO films.

### Data availability

The 4D-STEM data presented in this study are available in Zenodo <https://doi.org/10.5281/zenodo.18373896>.

### Code availability

The code for MEP is available Zenodo <https://doi.org/10.5281/zenodo.18373896>.

### References

- Cheema, S. S. et al. Enhanced ferroelectricity in ultrathin films grown directly on silicon. *Nature* **580**, 478–482 (2020).
- Kang, S. et al. Highly enhanced ferroelectricity in HfO<sub>2</sub>-based ferroelectric thin film by light ion bombardment. *Science* **376**, 731–738 (2022).
- Luo, Q. et al. A highly CMOS compatible hafnia-based ferroelectric diode. *Nat. Commun.* **11**, 1391 (2020).
- Müller, J. et al. Ferroelectricity in Simple Binary ZrO<sub>2</sub> and HfO<sub>2</sub>. *Nano Lett.* **12**, 4318–4323 (2012).
- Yan, F. J. et al. Recent progress on defect-engineering in ferroelectric HfO<sub>2</sub>: The next step forward multiscale structural optimization. *Mater. Horiz.* **11**, 626–645 (2024).
- Yang, W. et al. Ferroelectricity of hafnium oxide-based materials: Current status and future prospects from physical mechanisms to device applications. *J. Semiconductors* **44**, 053101 (2023).
- Schroeder, U., Park, M. H., Mikolajick, T. & Hwang, C. S. The fundamentals and applications of ferroelectric HfO<sub>2</sub>. *Nat. Rev. Mater.* **7**, 670–670 (2022).
- Ihlefeld, J. F., Jaszewski, S. T. & Fields, S. S. A Perspective on ferroelectricity in hafnium oxide: Mechanisms and considerations regarding its stability and performance. *Appl. Phys. Lett.* **121**, 40502 (2023).
- Khan, A. I., Keshavarzi, A. & Datta, S. The future of ferroelectric field-effect transistor technology. *Nat. Electron.* **3**, 588–597 (2020).

10. Kim, K. H., Karpov, I., Olsson, R. H. 3rd & Jariwala, D. Wurtzite and fluorite ferroelectric materials for electronic memory. *Nat. Nanotechnol.* **18**, 422–441 (2023).
11. Hoffmann, M. et al. Unveiling the double-well energy landscape in a ferroelectric layer. *Nature* **565**, 464–467 (2019).
12. Cheng, Y. et al. Reversible transition between the polar and antipolar phases and its implications for wake-up and fatigue in HfO<sub>2</sub>-based ferroelectric thin film. *Nat. Commun.* **13**, 645 (2022).
13. Li X. et al. Ferroelastically protected reversible orthorhombic to monoclinic-like phase transition in ZrO<sub>2</sub> nanocrystals. *Nature Materials* (2024).
14. Kumar, P., Gupta, D. & Lee, J. H. Negative Gradient Energy Facilitates Charged Domain Walls in HfO<sub>2</sub>. *Phys. Rev. Lett.* **134**, 166101 (2025).
15. Yang, J. et al. Theoretical Lower Limit of Coercive Field in Ferroelectric Hafnia. *Phys. Rev. X* **15**, 021042 (2025).
16. Xu Z., Zhu X., Zhao G.-D., Zhang D. W., Yu S. Oxygen vacancies stabilized 180° charged domain walls in ferroelectric hafnium oxide. *Applied Physics Letters* **124** (2024).
17. Paul, T. K., Saha, A. K. & Gupta, S. K. Formation and energetics of head-to-head and tail-to-tail domain walls in hafnium zirconium oxide. *Sci. Rep.-Uk* **14**, 9861 (2024).
18. He, R., Wu, H. Y., Liu, S., Liu, H. F. & Zhong, Z. C. Ferroelectric structural transition in hafnium oxide induced by charged oxygen vacancies. *Phys. Rev. B* **104**, L180102 (2021).
19. Wu, Y. et al. Unconventional Polarization-Switching Mechanism in (Hf, Zr)O<sub>2</sub> Ferroelectrics and Its Implications. *Phys. Rev. Lett.* **131**, 226802 (2023).
20. Lee, H. J. et al. Scale-free ferroelectricity induced by flat phonon bands in HfO<sub>2</sub>. *Science* **369**, 1343–1347 (2020).
21. Li, X. et al. Polarization Switching and Correlated Phase Transitions in Fluorite-Structure ZrO<sub>2</sub> Nanocrystals. *Adv. Mater.* **35**, e2207736 (2023).
22. Nukala, P. et al. Reversible oxygen migration and phase transitions in hafnia-based ferroelectric devices. *Science* **372**, 630–635 (2021).
23. Sang, X. H., Grimley, E. D., Schenk, T., Schroeder, U. & LeBeau, J. M. On the structural origins of ferroelectricity in HfO<sub>2</sub> thin films. *Appl. Phys. Lett.* **106**, 126905 (2015).
24. Grimley, E. D., Schenk, T., Mikolajick, T., Schroeder, U. & LeBeau, J. M. Atomic Structure of Domain and Interphase Boundaries in Ferroelectric HfO<sub>2</sub>. *Adv. Mater. Interfaces* **5**, 1701258 (2018).
25. Boescke, T. S., Müller, J., Bräuhaus, D., Schröder, U. & Böttger, U. Ferroelectricity in hafnium oxide thin films. *Appl. Phys. Lett.* **99**, 102903 (2011).
26. Yu, C. et al. Insights into the origin of robust ferroelectricity in HfO<sub>2</sub>-based thin films from the order-disorder transition driven by vacancies. *Phys. Rev. Appl.* **22**, 024028 (2024).
27. Wang, Y. et al. A stable rhombohedral phase in ferroelectric Hf(Zr)<sub>1-x</sub>O<sub>2</sub> capacitor with ultralow coercive field. *Science* **381**, 558–563 (2023).
28. Nukala, P., Wei, Y. F., de Haas, V., Guo, Q. K., Antoja-Leonart, J. & Noheda, B. Guidelines for the stabilization of a polar rhombohedral phase in epitaxial Hf<sub>0.5</sub>Zr<sub>0.5</sub>O<sub>2</sub> thin films. *Ferroelectrics* **569**, 148–163 (2020).
29. Wei, Y. et al. A rhombohedral ferroelectric phase in epitaxially strained Hf<sub>0.5</sub>Zr<sub>0.5</sub>O<sub>2</sub> thin films. *Nat. Mater.* **17**, 1095–1100 (2018).
30. Zhong, H. et al. Large-Scale Hf<sub>0.5</sub>Zr<sub>0.5</sub>O<sub>2</sub> Membranes with Robust Ferroelectricity. *Adv. Mater.* **34**, e2109889 (2022).
31. Zheng Y. Z. et al. Atomic-scale characterization of defects generation during fatigue in ferroelectric Hf<sub>0.5</sub>Zr<sub>0.5</sub>O<sub>2</sub> films: vacancy generation and lattice dislocation. *Int El Devices Meet.* 33.35.31-33.35.34 (2021).
32. Chen, L., Liang, Z., Shao, S., Huang, Q., Tang, K. & Huang, R. First direct observation of the built-in electric field and oxygen vacancy migration in ferroelectric Hf<sub>0.5</sub>Zr<sub>0.5</sub>O<sub>2</sub> film during electrical cycling. *Nanoscale* **15**, 7014–7022 (2023).
33. Gao, P. et al. Ferroelastic domain switching dynamics under electrical and mechanical excitations. *Nat. Commun.* **5**, 3801 (2014).
34. Gao, P. et al. Possible absence of critical thickness and size effect in ultrathin perovskite ferroelectric films. *Nat. Commun.* **8**, 15549 (2017).
35. Findlay, S. D., Azuma, S., Shibata, N., Okunishi, E. & Ikuhara, Y. Direct oxygen imaging within a ceramic interface, with some observations upon the dark contrast at the grain boundary. *Ultramicroscopy* **111**, 285–289 (2011).
36. Lazić, I., Bosch, E. G. T. & Lazar, S. Phase contrast STEM for thin samples: Integrated differential phase contrast. *Ultramicroscopy* **160**, 265–280 (2016).
37. Jia, C. L., Lentzen, M. & Urban, K. Atomic-Resolution Imaging of Oxygen in Perovskite Ceramics. *Science* **299**, 870–873 (2003).
38. Gao, P., Kumamoto, A., Ishikawa, R., Lugg, N., Shibata, N. & Ikuhara, Y. Picometer-scale atom position analysis in annular bright-field STEM imaging. *Ultramicroscopy* **184**, 177–187 (2018).
39. LeBeau, J. M., Findlay, S. D., Allen, L. J. & Stemmer, S. Position averaged convergent beam electron diffraction: Theory and applications. *Ultramicroscopy* **110**, 118–125 (2010).
40. Yadav, A. K. et al. Spatially resolved steady-state negative capacitance. *Nature* **565**, 468–471 (2019).
41. Ophus, C. Four-Dimensional Scanning Transmission Electron Microscopy (4D-STEM): From Scanning Nanodiffraction to Ptychography and Beyond. *Microsc. Microanalysis* **25**, 563–582 (2019).
42. Deb P. et al. Imaging Polarity in Two Dimensional Materials by Breaking Friedel’s Law. *Ultramicroscopy* **215** (2020).
43. Jiang, Y. et al. Electron ptychography of 2D materials to deep sub-angstrom resolution. *Nature* **559**, 343–349 (2018).
44. Odstrcil, M., Menzel, A. & Guizar-Sicairos, M. Iterative least-squares solver for generalized maximum-likelihood ptychography. *Opt. Express* **26**, 3108–3123 (2018).
45. Schloz, M., Pekin, T. C., Chen, Z., Van den Broek, W., Muller, D. A. & Koch, C. T. Overcoming information reduced data and experimentally uncertain parameters in ptychography with regularized optimization. *Opt. Express* **28**, 28306–28323 (2020).
46. Chen, Z. et al. Electron ptychography achieves atomic-resolution limits set by lattice vibrations. *Science* **372**, 826–831 (2021).
47. Sha, H., Cui, J. & Yu, R. Deep sub-angstrom resolution imaging by electron ptychography with misorientation correction. *Sci. Adv.* **8**, eabn2275 (2022).
48. Sha, H. et al. Sub-nanometer-scale mapping of crystal orientation and depth-dependent structure of dislocation cores in SrTiO<sub>3</sub>. *Nat. Commun.* **14**, 162 (2023).
49. Yang, H. et al. Simultaneous atomic-resolution electron ptychography and Z-contrast imaging of light and heavy elements in complex nanostructures. *Nat. Commun.* **7**, 12532 (2016).
50. Maiden, A. M., Humphry, M. J. & Rodenburg, J. M. Ptychographic transmission microscopy in three dimensions using a multi-slice approach. *J. Opt. Soc. Am. A Opt. Image Sci. Vis.* **29**, 1606–1614 (2012).
51. Maiden, A. M. & Rodenburg, J. M. An improved ptychographical phase retrieval algorithm for diffractive imaging. *Ultramicroscopy* **109**, 1256–1262 (2009).
52. Li, P., Edo, T., Batey, D., Rodenburg, J. & Maiden, A. Breaking ambiguities in mixed state ptychography. *Opt. Express* **24**, 9038–9052 (2016).
53. Chen Z. et al. Mixed-state electron ptychography enables sub-angstrom resolution imaging with picometer precision at low dose. *Nature Communications* **11** (2020).
54. Chen, Z., Shao, Y.-T., Jiang, Y. & Muller, D. Three-dimensional imaging of single dopants inside crystals using multislice electron ptychography. *Microsc. Microanalysis* **27**, 2146–2148 (2021).

55. Sha, H. et al. Ptychographic measurements of varying size and shape along zeolite channels. *Sci. Adv.* **9**, eadf1151 (2023).
56. Dong Z. et al. Visualization of oxygen vacancies and self-doped ligand holes in  $\text{La}_3\text{Ni}_2\text{O}_{7-\delta}$ . *Nature*, 1-6 (2024).
57. Zhang, Y., Chen, H. X., Duan, L., Fan, J. B., Ni, L. & Ji, V. A comparison study of the Born effective charges and dielectric properties of the cubic, tetragonal, monoclinic, ortho-I, ortho-II and ortho-III phases of zirconia. *Solid State Sci.* **81**, 58–65 (2018).
58. Materlik, R. C. K., A. Kersch The Origin of Ferroelectricity in  $\text{Hf}_x\text{Zr}_{1-x}\text{O}_2$ : A Computational Investigation and a Surface Energy Model. *J. Appl. Phys.* **117**, 134109 (2015).
59. Lowther, J. E., Dewhurst, J. K., Leger, J. M. & Haines, J. Relative stability of  $\text{ZrO}_2$  and  $\text{HfO}_2$  structural phases. *Phys. Rev. B* **60**, 14485–14488 (1999).
60. Kisi, E. H., Howard, C. J. & Hill, R. J. Crystal-Structure of Orthorhombic Zirconia in Partially Stabilized Zirconia. *J. Am. Ceram. Soc.* **72**, 1757–1760 (1989).
61. Ohtaka, O., Yamanaka, T., Kume, S., Hara, N., Asano, H. & Izumi, F. Structural-Analysis of Orthorhombic  $\text{ZrO}_2$  by High-Resolution Neutron Powder Diffraction. *P Jpn Acad. B-Phys.* **66**, 193–196 (1990).
62. Qi, Y. et al. Stabilization of Competing Ferroelectric Phases of  $\text{HfO}_2$  under Epitaxial Strain. *Phys. Rev. Lett.* **125**, 257603 (2020).
63. Ramanathan, S., Muller, D. A., Wilk, G. D., Park, C. M. & McIntyre, P. C. Effect of oxygen stoichiometry on the electrical properties of zirconia gate dielectrics. *Appl. Phys. Lett.* **79**, 3311–3313 (2001).
64. Stemmer, S., Chen, Z. Q., Zhu, W. J. & Ma, T. P. Electron energy-loss spectroscopy study of thin film hafnium aluminates for novel gate dielectrics. *J. Microsc.* **210**, 74–79 (2003).
65. Calka, P. et al. Chemical and structural properties of conducting nanofilaments in  $\text{TiN}/\text{HfO}_2$ -based resistive switching structures. *Nanotechnology* **24**, 085706 (2013).
66. Zhou, Y. et al. The effects of oxygen vacancies on ferroelectric phase transition of  $\text{HfO}_2$ -based thin film from first-principle. *Computational Mater. Sci.* **167**, 143–150 (2019).
67. Lee, J. et al. Role of oxygen vacancies in ferroelectric or resistive switching hafnium oxide. *Nano Convergence* **10**, 55 (2023).
68. Chisholm, M. F., Luo, W., Oxley, M. P., Pantelides, S. T. & Lee, H. N. Atomic-scale compensation phenomena at polar interfaces. *Phys. Rev. Lett.* **105**, 197602 (2010).
69. Kim, S. J., Mohan, J., Summerfelt, S. R. & Kim, J. Ferroelectric  $\text{Hf}_{0.5}\text{Zr}_{0.5}\text{O}_2$  Thin Films: A Review of Recent Advances. *Jom* **71**, 246–255 (2018).
70. Cheema, S. S. et al. Ultrathin ferroic  $\text{HfO}_2$ - $\text{ZrO}_2$  superlattice gate stack for advanced transistors. *Nature* **604**, 65–71 (2022).
71. Li, M. et al. Direct observation of weakened interface clamping effect enabled ferroelastic domain switching. *Acta Mater.* **171**, 184–189 (2019).
72. Jia, C.-L., Mi, S.-B., Urban, K., Vrejoiu, I., Alexe, M. & Hesse, D. Atomic-scale study of electric dipoles near charged and uncharged domain walls in ferroelectric films. *Nat. Mater.* **7**, 57–61 (2008).
73. Bednyakov, P. S., Sturman, B. I., Sluka, T., Tagantsev, A. K. & Yudin, P. V. Physics and applications of charged domain walls. *Npj Comput Mater.* **4**, 65 (2018).
74. Junquera, J. & Ghosez, P. Critical thickness for ferroelectricity in perovskite ultrathin films. *Nature* **422**, 506–509 (2003).
75. Ahn, C. H., Rabe, K. M. & Triscone, J.-M. Ferroelectricity at the Nanoscale: Local Polarization in Oxide Thin Films and Heterostructures. *Science* **303**, 488–491 (2004).
76. Zhou P. A. et al. Intrinsic 90° charged domain wall and its effects on ferroelectric properties. *Acta Mater* **232** (2022).
77. Zheng Y. Z. et al. Direct atomic-scale visualization of the 90° domain walls and their migrations in  $\text{Hf}_{0.5}\text{Zr}_{0.5}\text{O}_2$  ferroelectric thin films. *Mater Today Nano* **24** (2023).
78. Yang, W., Sha, H., Cui, J., Mao, L. & Yu, R. Local-orbital ptychography for ultrahigh-resolution imaging. *Nat. Nanotechnol.* **19**, 612–617 (2024).
79. Wakonig, K. et al. PtychoShelves, a versatile high-level framework for high-performance analysis of ptychographic data. *J. Appl Crystallogr* **53**, 574–586 (2020).
80. Silinga A., Allen C., Barthel J., Ophus C., MacLaren I. Measurement of Atomic Modulation Direction Using the Azimuthal Variation of First-Order Laue Zone Electron Diffraction. *Microscopy and micro-analysis: the official journal of Microscopy Society of America, Microbeam Analysis Society, Microscopical Society of Canada* **29** (2023).
81. Ziatdinov, M., Ghosh, A., Wong, C. Y. & Kalinin, S. V. AtomAI framework for deep learning analysis of image and spectroscopy data in electron and scanning probe microscopy. *Nat. Mach. Intell.* **4**, 1101–1112 (2022).
82. Nord, M., Vullum, P. E., MacLaren, I., Tybell, T. & Holmestad, R. Atomap: a new software tool for the automated analysis of atomic resolution images using two-dimensional Gaussian fitting. *Adv. Struct. Chem. Imaging* **3**, 9 (2017).
83. Cohen, R. E. Origin of ferroelectricity in perovskite oxides. *Nature* **358**, 136–138 (1992).
84. Mukherjee, B., Fedorova, N. S. & Íñiguez-González, J. First-principles predictions of  $\text{HfO}_2$ -based ferroelectric superlattices. *Npj Comput Mater.* **10**, 153 (2024).
85. Tariq A. First-principle calculations of ferroelectric properties of  $\text{HfO}_2$  and  $\text{ZrO}_2$ . (2022).
86. Madsen, J. & Susi, T. The abTEM code: transmission electron microscopy from first principles. *Open Res. Eur.* **1**, 24 (2021).
87. Momma, K. & Izumi, F. VESTA 3 for three-dimensional visualization of crystal, volumetric and morphology data. *J. Appl. Crystallogr.* **44**, 1272–1276 (2011).

## Acknowledgements

This work was supported by the National Natural Science Foundation of China (52125307 to P.G., 12222414 to C.G., 12504198 to J.D.) and the open research fund of Song-shan Lake Materials Laboratory (2022SLABFK03). P.G. acknowledges the support from the New Cornerstone Science Foundation through the XPLOER PRIZE. We acknowledge Electron Microscopy Laboratory of Peking University for the use of electron microscopes and High-performance Computing Platform of Peking University for providing computational resources. We acknowledge the assistance of Prof. Zhen Chen from Beijing National Laboratory for Condensed Matter Physics, Institute of Physics, Chinese Academy of Sciences, Beijing, China; We thank the discussion of Yi Jiang from the Advanced Photon Source, Argonne National Laboratory, USA.

## Author contributions

P.G. conceived the project. X.Y.G. performed the ptychographic experiments, reconstruction and data analyses with the assistance of B.H., R.L.M., R.C.S., R.X.Z., J.B.L., T.W., and J.D.L.; X.W.Z. performed the STEM-EELS experiment and analysis. Z.H.L., K.J.J., and C.G. prepared the HZO sample. X.Y.G. wrote the manuscript under the direction of J.D.L. and P.G.; All the authors contributed to this work through useful discussion and/or comments to the manuscript.

## Competing interests

The authors declare no competing interest

## Additional information

**Supplementary information** The online version contains supplementary material available at <https://doi.org/10.1038/s41467-026-69514-w>.

**Correspondence** and requests for materials should be addressed to Jiade Li, Chen Ge or Peng Gao.

**Peer review information** *Nature Communications* thanks Andreas Beyer, Woonbae Sohn, Maxime Le Ster and the other anonymous reviewer(s) for their contribution to the peer review of this work. A peer review file is available.

**Reprints and permissions information** is available at <http://www.nature.com/reprints>

**Publisher's note** Springer Nature remains neutral with regard to jurisdictional claims in published maps and institutional affiliations.

**Open Access** This article is licensed under a Creative Commons Attribution-NonCommercial-NoDerivatives 4.0 International License, which permits any non-commercial use, sharing, distribution and reproduction in any medium or format, as long as you give appropriate credit to the original author(s) and the source, provide a link to the Creative Commons licence, and indicate if you modified the licensed material. You do not have permission under this licence to share adapted material derived from this article or parts of it. The images or other third party material in this article are included in the article's Creative Commons licence, unless indicated otherwise in a credit line to the material. If material is not included in the article's Creative Commons licence and your intended use is not permitted by statutory regulation or exceeds the permitted use, you will need to obtain permission directly from the copyright holder. To view a copy of this licence, visit <http://creativecommons.org/licenses/by-nc-nd/4.0/>.

© The Author(s) 2026